J. Mech. Phys. Solids 178 (2023) 105331

Contents lists available at ScienceDirect

Journal of the Mechanics and Physics of Solids

journal homepage: www.elsevier.com/locate/jmps

Grain size and shape dependent crystal plasticity finite element model and its application to electron beam welded SS316L

Eralp Demir [a,*], Edward W. Horton [b], Mehdi Mokhtarishirazabad [b], Mahmoud Mostafavi [b], David Knowles [b]

[a] Department of Engineering Science, University of Oxford, Parks road, Oxford OX1 3PJ, UK
[b] Department of Mechanical Engineering, University of Bristol, Bristol, BS8 1TR, UK

ARTICLE INFO

Keywords:
Crystal plasticity
Finite element method
Electron beam welding
Grain size
Morphological and crystallographic texture
Ellipsoids

ABSTRACT

Electron beam welding is an autogenous welding process that leads to microstructural heterogeneities; crystallographic texture, elongated and larger grain size relative to the surrounding parent material. The goal of this study is to predict the changes in mechanical response of the weld fusion zone as a function of grain morphology and texture by using the parent material properties to avoid extensive and costly experimental campaigns. For this reason, a crystal plasticity solver, "University of **BRI**stol cry**S**tal plas**T**icity s**OL**ver" (**BRISTOL**), is implemented in a finite element framework with new constitutive laws to account for the length-scale dependence considering the size and shape of the grains. It is found that the crystallographic texture governs the orientation specific elastic stiffness and yield stress having the most dominant effect on the macroscopic response of the weldment at the grain size scales considered. Crucially the length-scale dependent model allows accurate prediction of the yield strength of the weldment over a range of microstructures, also highlighting the presence of other factors such as prior strain hardening during the welding process and residual stresses.

1. Introduction

Electron beam welding (EBW) is being considered for use in the nuclear industry for joining key components because of its potential for high productivity and efficiency. Besides the beneficial characteristic features of EBW; uniform energy density and narrow heat affected zone, EBW can lead to relatively low residual stresses and distortion (Chowdhury et al., 2018). EBW can join thick pieces togehter with uniform chemistry (Vasileiou et al., 2017) but it can result in significantly different crystallographic texture in the weldment zone which give rise to highly directional properties. In addition, grain growth results in a morphological texture, significantly elongated and relatively large grains in comparison to the parent (conventionally manufactured) material (Wu et al., 2016; Das et al., 2021). These microstructural features have previously been measured to generate realistic polycrystal representations for simulations in order to predict the mechanical response (i.e. stiffness, yield strength, strain hardening behavior, and residual stresses) of weldments or additively manufactured materials (Kapoor et al., 2018).
Crystal plasticity-based finite element (CPFEM) approaches have been used extensively for prediction of microstructure sensitive mechanical properties at a local grain level. Furthermore, dislocation density based models have been used to incorporate temperature dependent aspects in constitutive laws; such as thermally-activated glide, cross-slip, dipole formation, etc. (Ardeljan et al., 2014). Current focus has been the application of CPFEM together with artificial neural-networks, machine-learning and uncertainty quantification within the scope of data-driven modeling and simulation (Karapiperis et al., 2021).

* Corresponding author.
E-mail address: eralp.demir@eng.ox.ac.uk (E. Demir).

https://doi.org/10.1016/j.jmps.2023.105331
Received 11 January 2023; Received in revised form 14 April 2023; Accepted 23 May 2023
Available online 1 June 2023

The length-scale dependence of deformation such as yield strength has been a long-standing issue in understanding and modeling mechanical behavior of metals (Hutchinson, 2000). The physical source of the length-scale dependence was linked with the presence of grain boundaries in polycrystals, multi-phase, hard phase particles, dislocation cell substructures (Fleck et al., 1994). All these affect the mean-free-path of dislocations correlated to the strength through Taylor's relation for the dislocation strength (Roters et al., 2000).

A polycrystal aggregate behavior differs from the responses of columnar grains or surface grains due to the compatibility and equilibrium constraints imposed by the neighboring grains (Kocks and Mecking, 2003). Therefore, a surface grain cannot really represent bulk polycrystal behavior. Oligocrystal (few crystal) (Zhao et al., 2008; Demir and Gutierrez-Urrutia, 2021) and bi-crystal studies (Zaefferer et al., 2003) were useful to understand grain boundary behavior while those may not reflect the true polycrystal material behavior because the relatively different stress states of grains than a grain constrained in a polycrystal aggregate. For this reason crystal plasticity-based finite element simulation is an essential tool to accurately represent the stress states in the polycrystals. Currently there is software available (e.g. Dream3D and Neper) to generate representative volume elements (RVEs) for crystal plasticity. Experimental measurements such as grain size, aspect ratio of grains, or crystal orientations could enter as inputs to these synthetic microstructure generator tools to create an RVE directly from 2D or 3D microstructure maps. Accordingly, Dream3D® has the capability to create RVEs with hexahedron elements using flexible statistical tools for grain size and orientation distribution (Groeber and Jackson, 2014). Similarly, Neper® uses tessellation method that reveals grains with continuous edges and element type can be defined hexahedron or tetrahedrons (Quey et al., 2011). Investigations on the RVE selection by using those microstructure generators have been conducted recently (Lim et al., 2019; Chen et al., 2022). The RVE size and resolution were identified as the two important factors that significantly effect the convergence of Von Mises stress which is also a funcion of the applied strain (Lim et al., 2019). Accordingly, the average value of engineering stresses over an RVE, differ almost 100% through ramping up the total number of grains in the RVE from 10 to 1000 (Chen et al., 2022).

The Hall–Petch method is an empirical approach to correlate the inverse square root of the grain size to the mechanical yield strength (Hall, 1954). The experimental macroscopic yield stresses correlate reasonably well with the inverse square root of the magnitude of the grain size (Hansen, 2004). Therefore, the Hall–Petch equation has been used to incorporate grain size dependence for polycrystal models in various crystal plasticity frameworks (Mu et al., 2014; Liu et al., 2020).

Strain gradients have been used to incorporate the length-scale into crystal plasticity. Slip gradients were expressed in terms of Geometrically Necessary Dislocations (GND) to correlate with the flow strength of grains through the Taylor relation (Fleck et al., 1994). This method has been implemented in crystal plasticity-based finite element models to incorporate length-scale dependence (Dai, 1997). Therefore, dislocation density based constitutive laws that use GNDs as state variables were developed (Arsenlis and Parks, 2002; Cheong et al., 2005). Polycrystal models that were based on slip gradients and micro forces allowed modeling size dependence including backstress effects (Klusemann and Yalçinkaya, 2013; Yalçinkaya et al., 2021). Strain gradient models that were used in conjunction with crystal plasticity-based finite element framework had various applications; i.e. plastic behavior of bi-crystals (Liang and Dunne, 2009) and slip hardening interactions for a multi-phase alloys (Lu et al., 2020; Sun et al., 2019b). Among the many strain gradient models, only a few consistently update GNDs (Evers et al., 2004; Ma, 2006; Gerken and Dawson, 2008) using a non-local iterative loop to ensure consistency condition.

Gurtin's microstress model (Gurtin, 2002) has been used to incorporate long-range stress or backstress effects due to GNDs. Accordingly, a mean-field approach was developed (Acharya and Roy, 2006) and used in conjunction with a J2 model to predict distribution of dislocations (Arora and Acharya, 2020). Strain gradient approaches using slip rates as a separate field variable and that relied on macro and micro force equilibrium were also available to model length-scale size dependence (Niordson and Kysar, 2014). A similar micro-stress approach was used for backstress to predict shear banding of copper-niobium laminate (Zecevic et al., 2023). The strain-gradient formulation revealed an increase in the yield stress as a function of size (Wulfinghoff et al., 2015).

Less intricate approaches than strain gradient models were introduced to incorporate grain size effects. For example, a grain size dependent yield function with a phenomenological expression was used as a relatively simple alternative model to the strain gradient models (Cruzado et al., 2018). Similarly, a physically-based relationship was used through correlating grain size to the mean-free-path of dislocations to include the grain size dependence of flow stress (Haouala et al., 2018). Accordingly, a grain size dependent flow stress model to correlate slip resistance to the slip distance at the nearest neighbor grain and as a function of misorientation between the grains was employed recently to predict the non-local size dependent behavior of grains (Agius et al., 2022). However, this method suffered from the requirement of a large RVE due to consideration of adjacent grains which hinders the calibration process.

In this study, a length-scale dependent model is developed and implemented in a crystal plasticity-based framework to predict mechanical properties of stainless steel 316L weldment. The aim of this study is to predict the mechanical properties of the weldment using experimental data available for the non-welded (parent) material thereby to avoid rigorous and costly experiments to qualify the weldment. In the proposed model, grain dimensions are determined in a unique way through fitting ellipsoids to each grain hence the effect of grain morphology and grain size on the slip distance are both represented in the model. The proposed approach reveals an increase in the initial yield strength of the smaller grains unlike strain gradient models that require prior slip to get strengthening from the length-scale dependent strain hardening. In addition, a unique projection is used to compute the length-scale parameter defining the effect of grain size on each slip system considering the grain morphology. The model findings are compared to the experimental macroscopic mechanical response considering crystallographic and morphological aspects of texture in the weldment to better understand the major factors that control the mechanical behavior in a weldment.

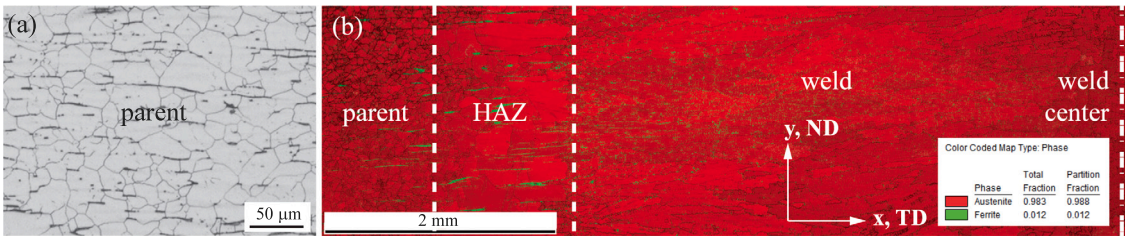

Fig. 1. (a) Parent material microstructure of SS316L after electrolytic etching in nitric acid 60% at 1 Volt for 60 s. The microstructure consists of austenite matrix (regions with high contrast - white) with traces of retained δ-ferrite (regions with low contrast - black), (b) parent and weld phase map.

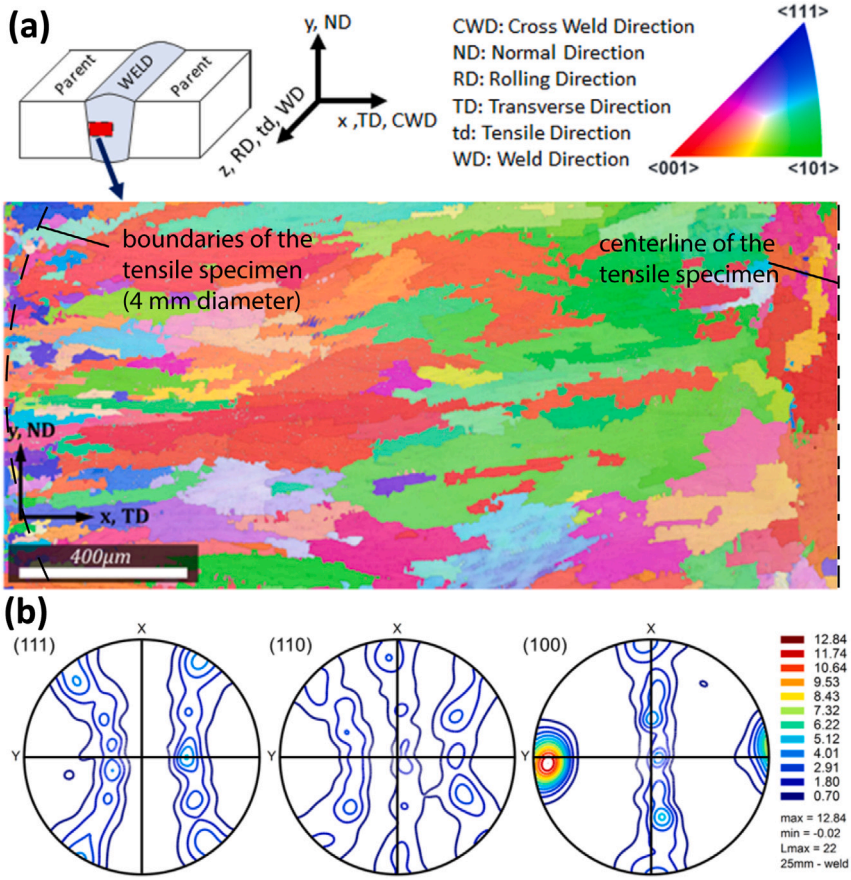

Fig. 2. (a) Inverse Pole Figure map of electron beam welded sample. The cross-section of the test sample of the weldment is indicated with the black dash line., (b) pole figures about RD.

2. Experiments

In this study, two plates of austenitic stainless steel type 316L (SS316L) with dimensions of 400 mm by 100 mm and thickness of 25.4 mm were welded using autogeneous electron beam welding (EBW). The welding parameters and details of manufacturing can be found elsewhere (Mokhtarishirazabad et al., 2019). The microstructural features of the parent metal and fusion zone were revealed by electrolytic etching (nitric acid 60% under 1 V for 60 s) of a ground and polished sample, cut from the weld cross-section, Fig. 1(a). The width of the fusion zone was about 4 mm. Optical images were acquired using a Zeiss Imager M2. Grain size of the parent material was measured by analyzing the optical images taken from the etched specimen in accordance with ASTM E112 standard (ASTM-E112-13, 2017). The average grain size was measured to be 20 ± 8 μm in the parent material of SS316L that represents the equiaxed microstructure away from the weld using optical microscopy.

Fig. 1(b) shows the phase map of the parent and weld material. The retained δ-ferrite phase (BCC) in the weld was approximately 1% in the weldment and 2% in parent material, thereby highlighting the dominant phase as FCC austenite.

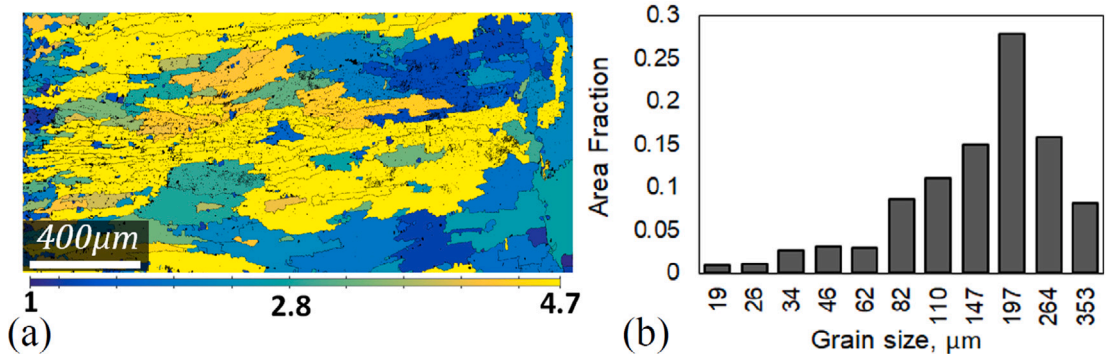

Fig. 3. (a) Grain aspect ratio distribution (A/B), and (b) grain size statistics obtained from the EBSD maps of the weldment. Plots are obtained using MTEX® software.

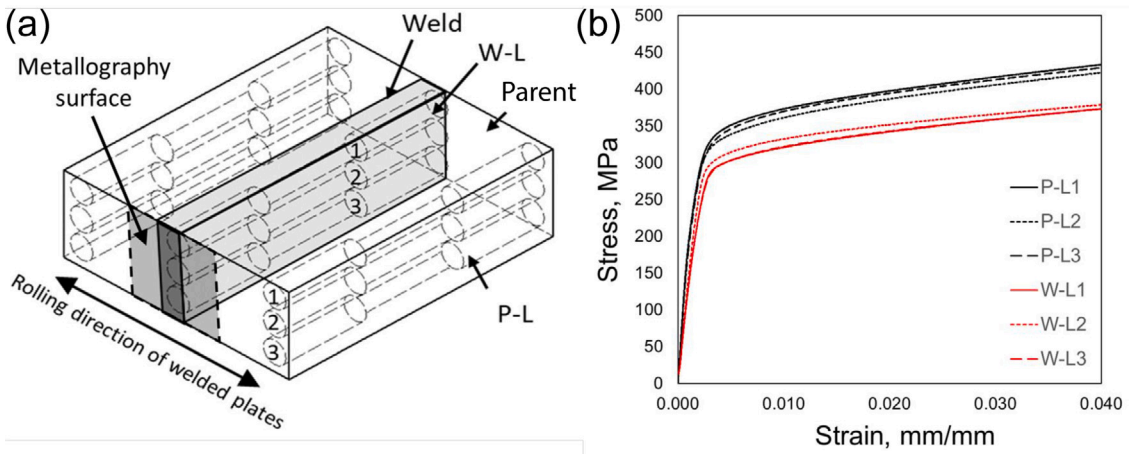

Fig. 4. (a) Schematic of the location of the tensile samples extracted from the EB welded plate and (b) the corresponding stress–strain curve for each sample.

The weld region of SS316L was ground and polished again to remove the etched surface before the EBSD analysis, Fig. 2(a). The final polishing was performed by a vibratory polisher for 12 h in 0.06 μm amorphous colloidal silica suspension (MasterMet by Buehler Ltd). Zeiss SigmaVP scanning electron microscope was employed for EBSD examination, working at 30 kV, while the specimen was tilted 70° with scanning step size of 2 μm. The weld region had a strong Cube and Goss texture indicated with the red and green colors respectively, in the inverse pole figure map in Fig. 2(b).

The average aspect ratio (AR) of the grains was obtained by using MTEX® software by fitting ellipses which are prescribed by the ratio of principal axes to the major axis A and B, Fig. 3(a). The grains with dimensions greater than 100 μm were considered in this analysis only. The aspect ratio of grains had a significant variation. Therefore, two different average aspect ratios were computed as 8.2 (for grains with $A/B \geq 5$) and 4.8 (for grains with $A/B < 5$). Similarly, the average grain sizes were measured as 392 ± 233 μm, Fig. 13(a), and 194 ± 233 μm, Fig. 13(b), respectively for the two aspect ratios.

Cross-head displacement-controlled tensile tests were performed on round samples extracted along the weld-line from the fusion zone and parent material using an Instron 5969 universal testing machine at a rate of 0.5 mm/min, following ASTM E8M (ASTM-E8, 2001). The elongation of the tensile samples was measured by mounting an axial clip-on extensometer on their gauge length. The gauge length and diameter of the specimens were 20 mm and 4 mm, respectively. Fig. 4 shows the location from which the tensile samples were extracted from the weldment and the corresponding stress–strain curve for each sample. Fig. 2(a) indicated the size and location of the longitudinally extracted samples on the EBSD map with the black circular dash line.

3. Method

This section includes a brief review of crystal plasticity, length-scale dependent constitutive laws, and the methodology used to model the shape and size of the grains, respectively.

Table 1
Slip vectors in the crystal reference frame for fcc materials; $\mathbf{s}^a$ and $\mathbf{n}^a$ denote slip direction and slip plane normal, respectively. The transverse direction, $\mathbf{t}^a$, is obtained by the cross-product of the slip direction and the slip plane normal.

$\mathbf{n}^a$	(111)			$(\bar{1}\bar{1}1)$			$(1\bar{1}\bar{1})$			$(\bar{1}1\bar{1})$		
$\mathbf{s}^a$	$[01\bar{1}]$	$[\bar{1}01]$	$[1\bar{1}0]$	$[0\bar{1}\bar{1}]$	[101]	$[\bar{1}10]$	$[0\bar{1}1]$	$[\bar{1}0\bar{1}]$	[110]	[011]	$[10\bar{1}]$	$[\bar{1}\bar{1}0]$

3.1. Crystal plasticity

The total deformation, $\mathbf{F}$, is decomposed into its elastic, $\mathbf{F^e}$, and volume conserving plastic, $\mathbf{F^p}$, parts using Eq. (1):

$$\mathbf{F} = \mathbf{F^e}\,\mathbf{F^p}, \quad \det(\mathbf{F^p}) = 1. \tag{1}$$

Green–Lagrange strain is used to calculate the elastic strain, $\mathbf{E^e}$ for large displacements from Eq. (2) in which $\mathbf{I}$ is the 2nd rank identity tensor:

$$\mathbf{E^e} = \frac{\mathbf{F^{e}}^T\,\mathbf{F^e} - \mathbf{I}}{2}. \tag{2}$$

$\mathbf{P}$ is 2nd Piola–Kirchoff (PK2) stress that is obtained using elasticity matrix of cubic crystal, $\mathbf{D}$, Eq. (3). Note that all of the calculations were performed in the crystal reference using the sample to crystal transformation in Appendix A that is explained in Appendix B:

$$\mathbf{P} = \mathbf{D} : \mathbf{E^e}. \tag{3}$$

Resolved shear stress on a slip system is obtained by projecting PK2 stress on the slip the systems. By assuming small elastic strains for metals, Eq. (4) is obtained:

$$\tau^a = \mathbf{F^{eT}}\,\mathbf{F^e}\,\mathbf{P} : \mathbf{S}^a \approx \mathbf{P} : \mathbf{S}^a. \tag{4}$$

Schmid tensor transforms the slip (simple shear) from respective slip system prescribed by its slip direction, $\mathbf{s}^a$, and slip plane normal, $\mathbf{n}^a$ which reveals the dyadic product in Eq. (5):

$$\mathbf{S}^a = \mathbf{s}^a \otimes \mathbf{n}^a. \tag{5}$$

Table 1 shows the slip direction and slip plane normals for FCC type materials. The parent and weld materials contain approximately 98% and 99% of austenite volume fraction with FCC structure. The retained δ-ferrite phase in the weldment had relatively low volume fraction (<1.2% of the overall), Fig. 1(b), hence only FCC structure was considered in this study.
The sum of the slip rates on each slip system using the corresponding shear transformation using Schmid tensor, $\mathbf{S}^a$, reveals the plastic velocity gradient, $\mathbf{L^p}$, Eq. (6):

$$\mathbf{L^p} = \sum_a \mathbf{S}^a \dot{\gamma}^a. \tag{6}$$

Cauchy stress, $\boldsymbol{\sigma}$, is calculated by transforming PK2 stress, $\mathbf{P}$, to the deformed configuration using Nanson's relation as in Eq. (7):

$$\boldsymbol{\sigma} = \mathbf{F^e}\,\mathbf{P}\,\mathbf{F^{e}}^T / \det \mathbf{F^e}. \tag{7}$$

The output quantities are computed at the end of the increment such as cumulative slip, Γ, according to Eq. (8):

$$\Gamma = \sum_a \int_0^t \dot{\gamma}^a \mathrm{d}t. \tag{8}$$

The two level semi-implicit crystal plasticity time integration scheme of Kalidindi et al. is adopted in this study (Kalidindi et al., 1992). The solution method is briefly explained in Appendix C.

3.2. Finite element solver

The crystal plasticity approach is implemented in a finite element framework in ABAQUS® with the user subroutine functions UMAT, UEXTERNALDB, and UVARM for defining the material mechanical response, to perform relevant initializations, and to output the results, respectively. UMAT returns the total deformation gradient while requesting two entries; the Cauchy stress ($\boldsymbol{\sigma}$) and material tangent stiffness ($\frac{\partial \boldsymbol{\sigma}}{\partial \mathbf{e}}$) in order to perform the displacement field iteration (Hibbitt et al., 2014).

The crystal plasticity solver, BRISTOL,[1] based on a semi-implicit solver for PK2 stress was developed during this study. The proposed apporach is completely different from the earlier crystal plasticity solver that was based on single level forward-gradient method based on the solution for the slip increments (Huang, 1991). A working version of BRISTOL with example input files, ABAQUS® environment files, and a user documentation is provided within this study. A maintained version will be available publicly

[1] Fortran implementation of this study is termed as **BRISTOL** that stands for "University of **BRI**stol cry**S**tal plas**T**icity s**OL**ver".

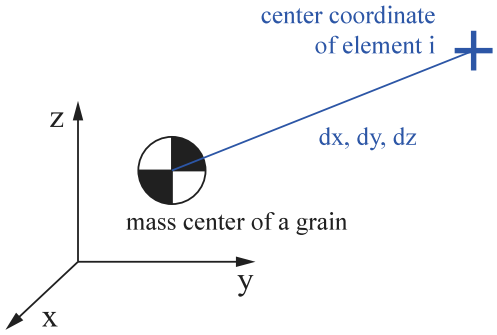

Fig. 5. Calculation of second moment of an element "i" about the centre of mass of a grain.

(https://github.com/smrg-uob). The two-level scheme and modular implementation allows a relatively easy way to develop new constitutive models compared to the single-level schemes that require all the differential terms including state variables.

The Jacobian (or material tangent) was computed analytically because the inefficiency of the perturbation method in that was outlined in the Ref. Kalidindi et al. (1992). To better explain that, for a material point crystal plasticity needs to be solved six more times in the case of perturbation making it inefficient. In addition, the perturbed strain increments, that are slightly larger than the total strain increments, that may give rise to convergence issues resulting in significant number of time cut-backs. For all these reasons, a slightly modified version of the analytical Jacobian in Ref. Balasubramanian (1995) and Lieou and Bronkhorst (2020) is implemented Appendix D.

3.3. Constitutive laws

The cubic elasticity matrix, **D**, was constructed using three independent constants C_{11}, C_{12}, and C_{44}. Power law was used to calculate slip rates per slip systems, $\dot{\gamma}^a$, because of its computational efficiency over more physics-based sine-hyperbolic or exponential laws, Eq. (9). $\dot{\gamma}_0$ and m were reference slip rate and rate sensitivity exponent that need to be determined by calibration:

$$\dot{\gamma}^a = \dot{\gamma}_0 \left(\frac{|\tau^a - X^a|}{\tau_c^a} \right)^{1/m} \operatorname{sign}(\tau^a - X^a). \tag{9}$$

The critical resolved shear stress (CRSS) is a function of initial strength, τ_c^0, and dislocation density, ϱ^a through Taylor's strength relation, Eq. (10). The length-scale term, L^a, incorporates the grain size dependent portion of strength on the slip systems through an adjusting parameter C:

$$\tau_c^a = \tau_c^0 + \alpha G b \left(\sqrt{\varrho^a} + \frac{C}{L^a} \right). \tag{10}$$

The model uses two state variables; dislocation density, ϱ^a,and backstress, X^a, for each slip system. The dislocation density evolution was governed by Kocks–Mecking type of strain hardening rule (Mecking and Kocks, 1981), Eq. (11), with hardening and softening parameters of K and y_c, respectively. y_c represents the temperature and strain-rate dependent annihilation events. The grain size dependence of strain hardening effects were introduced through the mean-free-path parameter, L^a, using the same scaling constant, C, as in the strength similar to Cruzado et al. (2018) and Haouala et al. (2018):

$$\dot{\varrho}^a = \left[K \left(\sqrt{\varrho^a} + \frac{C}{L^a} \right) - 2 y_c \varrho^a \right] \frac{|\dot{\gamma}^a|}{b}. \tag{11}$$

The length-scale parameter effects yield strength through Eq. (10), and strain hardening (or state evolution) through Eq. (11). The same constant, C, was used in both expressions for simplicity. The relative effect of the length-scale parameter on the yield strength and strain hardening are adjusted by the calibration factors α and K, respectively.

Backstress was defined as another state variable and its evolution rate, $\dot{X}^a$, for each slip system, a, is computed by Eq. (12). The phenomenological expression for the backstress allows relatively robust solution unlike other methods that require additional iterative loops (Zecevic et al., 2023).

$$\dot{X}^a = h \dot{\gamma}^a - h_D X^a |\dot{\gamma}^a|. \tag{12}$$

3.4. Grain size and shape

Initially, the elements that belong to each grain was obtained. Then the centre of mass of a grain was calculated simply by taking the average of the center coordinates of the finite elements or voxels that belong to that grain.

The second moment, $\mathbf{m}_i$, about the centre of mass of a grain was then calculated by Eq. (13) using the elements inside the grain and their centre coordinates. Fig. 5 shows the schematic sketch of centre of mass of a grain and an example finite element "i" within

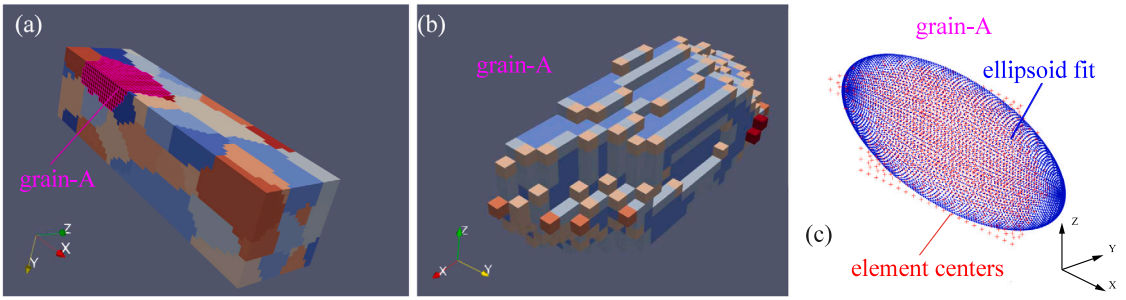

Fig. 6. Example ellipsoid fit to a grain with an aspect ratio of 5: (a) RVE and the selected grain (grain-A), (b) the finite elements in the selected grain, (c) the fitted ellipsoid (blue color) by using the centre coordinates of the elements of grain-A (red color).

that grain. dx, dy, and dz represent the moment arms from the centre of the element "i" to the centre of mass of the grain that the element belongs to:

$$\mathbf{m}_i = \begin{bmatrix} dx^2 & dxdy & dxdz \\ dydx & dy^2 & dydz \\ dzdx & dzdy & dz^2 \end{bmatrix}. \tag{13}$$

The second moments of each element of a grain were summed up to obtain the overall second moment tensor, $\mathbf{M}$ as in Eq. (14):

$$\mathbf{M} = \sum_i \mathbf{m}_i. \tag{14}$$

The eigenvalues, λ_k, of the second moment tensor reveal the principal dimensions of the ellipsoid while the eigenvectors, $\hat{\mathbf{d}}_k$, give the principal directions denoted with the subscript k using Eq. (15):

$$\left(\mathbf{M} - \lambda_k \mathbf{I}\right) \hat{\mathbf{d}}_k = \mathbf{0}. \tag{15}$$

Eq. (16) defines the ellipsoid orientation and dimensions. For example, the major (1st) axis of the ellipsoid is given by $\mathbf{d}_1 = \lambda_1 \hat{\mathbf{d}}_1$:

$$\mathbf{d}_k = \lambda_k \hat{\mathbf{d}}_k, \quad (k = 1, 2, 3). \tag{16}$$

Fig. 6 shows an example grain in a polycrystal RVE and the ellipsoid fit to that grain using the proposed approach. Various different geometries can be accurately represented using the ellipsoids. The principal axes of the ellipsoid need not necessarily coincide with the sample reference axes (X, Y, Z) meaning that the ellipsoid can be oriented in any direction.

The length-scale parameter for each slip system was obtained by using the component of the principal axes of the ellipsoid and the slip plane normals. The dislocation motion occurs by expansion of dislocation loops within the slip planes. Therefore, the projection Eq. (17) calculates the in-slip-plane components of the principal axes of the ellipsoids. This is similar to the projection for the irradiated dislocation loops in the Ref. Barton et al. (2013). The length-scale, L_i^a, for a grain with "i"th principal axis, $\mathbf{d}_i$, was computed using the projection in Eq. (17) to find the component of $\mathbf{d}_i$ vector on the slip plane, $\mathbf{n}^a$:

$$L_i^a = \left\| (\mathbf{I} - \mathbf{n}^a \otimes \mathbf{n}^a) \cdot \mathbf{d}_i \right\|. \tag{17}$$

The grain size effect was incorporated by the calculation of the effective slip distance individually for each slip system. The slip distance can be different depending on the orientation of the slip plane, $\mathbf{n}^a$, and on the shape of a grain (that is prescribed by an ellipsoid geometry with its principal axes in three directions, $\mathbf{d}_i$. Therefore, the projection in Eq. (17) was used to reveal the mean-free-path dimension on a slip system of a grain. Fig. 7 shows the projection schematically.

The projection in Eq. (17) takes into account the effect of grain dimensions along both the slip direction and transverse slip direction. Because slip shall be considered as the uniform expansion of a dislocation loop in all directions on the slip plane, considering the presence of both edge and screw type of dislocations.

Overall length-scale parameter was computed by using the norm of the length-scale projections for all of the principal directions, Eq. (18):

$$L^a = \sqrt{(L_1^a)^2 + (L_2^a)^2 + (L_3^a)^2}. \tag{18}$$

The length-scale analysis was performed only during initialization of the calculations. At first, the dimensions (eigenvalues) and principal directions (eigenvectors) of the ellipsoids for each grain were computed outside the finite element analysis(FEA) using MATLAB®. An input file for the FEA containing the principal axes of the ellipsoid fits in the sample reference, $\mathbf{d}_i$, along each principal direction for each grain was created. Note that, $\mathbf{d}_i$ were not unit vectors. For example, the length of $\mathbf{d}_1$ represents the dimension of the ellipsoid along its 1st principal axis. The projected lengths, L^a, for each slip system a and for each grain were

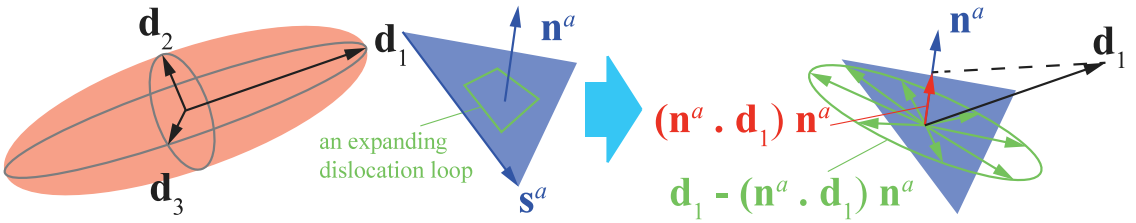

Fig. 7. Schematic sketch of a slip plane normal, $\mathbf{n}^a$, and an expanding dislocation loop. The projection is shown with for an example illustration for a grain with a principal axis vector $+\mathbf{d}_1$.

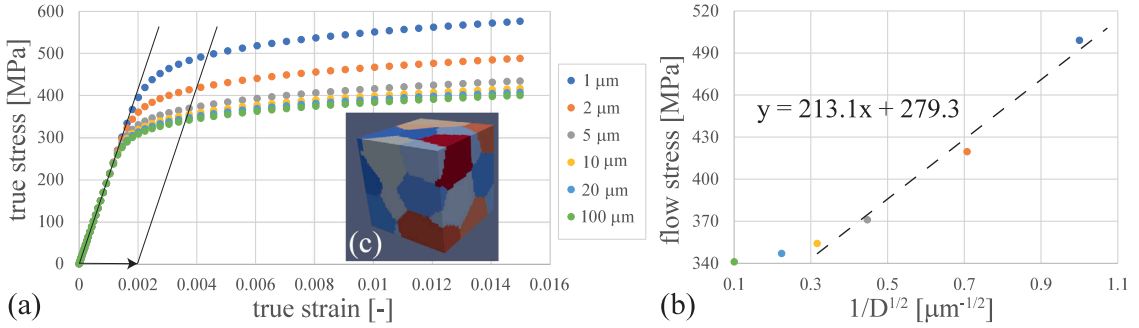

Fig. 8. Stress strain response for an equiaxed microstructure with various average grain sizes: 1 μm, 2 μm, 5 μm, 10 μm, 20 μm, and 100 μm. (a) stress–strain response up to 1.5% strain, (b) flow stress values obtained by 0.2% yield offset method, and (c) RVE with 40 × 40 × 40 grid with a total of 75 number of grains. Loading was along x-direction.

calculated within the initialization user subroutines once at the beginning of the crystal plasticity calculations. The same value of L^a was assigned to all integration points in the corresponding grain. The shape of the grains were insensitive to the deformation at low strains with tensile strains of 1.5%. However, the method can be generalized to large deformation processes.

The sensitivity of the model to the length-scale dependence of the grains was investigated by testing on an RVE with different average grain sizes. The RVE in Fig. 8(c) with 40 × 40 × 40 grids containing a total of 75 grains. The same RVE with different dimensional scaling was used in order eliminate the effect of the orientation scatter and grain geometries. Therefore the dimensions of the same RVE was scaled to give models with average grain sizes of 1 μm, 2 μm, 5 μm, 10 μm, 20 μm, and 100 μm. Fig. 8(a)–(b) show the engineering stress–strain curves that correspond to each grain and its extracted yield stresses using the yield-offset method, respectively. The length-scale dependence starts to become noticeable below 20 μm which is similar to the findings of Hall for mild-steel (Hall, 1954). Because the grain size becomes comparable to the mean-spacing of dislocations below this scale only. The value for the length-scale parameter, C, was found to be 10 based on the expected size scale transition below 20 μm grain size.

The yield strength in the proposed approach increases with decreasing grain size. The shift of yield strength is a salient feature of this model different from other strain gradient models. Because in strain gradient models, slip is required to develop slip gradients thereby leading to strain hardening or strengthening (Fleck and Hutchinson, 2001). The model presented here can reveal both the increase in the yield stress and the increase in strain hardening with a decrease in the grain dimensions.

4. Results and discussion

The effect of RVE resolution and RVE size on the stress–strain response was investigated using the equiaxed microstructure with uniform texture to check the representability of the RVE for the constitutive model used and for the strain levels considered in this study. The model was then used to simulate the tensile response of the weldment to further investigate the sensitivity of the results on the grain size statistics and crystallographic texture. The effect of pre-strains during welding process was approximately simulated and compared with the experimental response. Finally, the simulation results of the parent and weldment were analyzed.

The 3D synthetic microstructures were generated using Dream3D® software (Groeber and Jackson, 2014). Table 2 shows the properties of the different synthetic microstuctures that were used in the simulations. RVEs (0–6 and 10) represent the parent microstructure that were used to determine the RVE sensitivity to macroscopic stress. The remaining RVEs (7–9) were constructed using the microstructural properties of the weldment; using the statistics of grain size, morphological and crystallographic texture. RVE-7 neglects the presence of the crystallographic texture which was included in RVE-8 and RVE-9. The grains that were larger than 100 μm size were used to construct both RVE-8 and RVE-9. The grains with the aspect ratio greater than five (AR > 5) were selected for RVE-8 as shown in Fig. 13(a) while the grains with the smaller aspect ratio (AR < 5) were used for the grain size statistics of RVE-9, Fig. 13(b). This resulted in RVE-8 consisting of grains within the majority of the weld metal, while RVE-9 contains grains near the center-line of the weld. The minimum limit (min. lim.) of the grain size distribution restricts the size of the smallest grain

Table 2
Statistical parameters used with Dream3D® software. Average grain size (av. GS) and its standard deviation (std. GS) were the two major parameters. Equiaxed (equ.) and columnar (col.) indicates the grain morphology with the corresponding aspect ratios (AR). Voxel (vox.) size and number of divisions (div.) were uniform in all three directions. L, W, and H refer to the length width and height of the RVE along X, Y, and Z directions, respectively. The maximum (max. lim.) and minimum (min. lim.) limits represent the upper and lower cut-off values for the grain size distributions, respectively. Total number of grains (grain no.) and total number of finite elements (ele. no.) of each RVE are indicated.

RVE	Type	av. GS [μm]	std. GS [μm]	min. lim.	max. lim.	bin size	AR	vox. size	div.	ele. no.	L [μm]	W [μm]	H [μm]	Grain no.
0	equ.	20	8	0.15	0.04	1	1	1.25	32	32 768	40	40	40	26
1	equ.	20	8	0.15	0.04	1	1	2	20	8000	40	40	40	25
2	equ.	20	8	0.15	0.04	1	1	1	40	64 000	40	40	40	26
3	equ.	20	8	0.15	0.04	1	1	0.667	60	216 000	40	40	40	25
4	equ.	20	8	0.15	0.04	1	1	1.25	40	64 000	50	50	50	50
5	equ.	20	8	0.15	0.04	1	1	1.25	60	216 000	75	75	75	156
6	equ.	20	8	0.15	0.04	1	1	1.25	90	729 000	112.5	112.5	112.5	517
7	col.	392	233	0.001	0.1	50	8.2	30	80	512 000	2400	2400	2400	211
8	col.	392	233	0.001	0.1	50	8.2	30	80	512 000	2400	2400	2400	211
9	col.	194	117	0.001	0.1	20	4.8	30	80	512 000	2400	2400	2400	1760
10	equ.	20	8	0.15	0.04	1	1	1	80	512 000	80	80	80	189

Table 3
Calibrated model parameters and their description.

Description	Constant	Value	Unit
Cubic elastic constant	C_{11}	204.6×10^3	MPa
Cubic elastic constant	C_{12}	137.7×10^3	MPa
Cubic elastic constant	C_{44}	126.6×10^3	MPa
Burgers vector	b	0.256×10^{-6}	mm
Reference slip rate	$\dot{\gamma}_0$	0.01	s^{-1}
Rate sensitivity exp.	m	0.05	–
Initial slip strength	τ_c^0	75	MPa
Initial dislocation density	ϱ^0	3×10^7	$1/mm^2$
Hardening constant	K	0.035	–
Softening constant	y_c	0.6×10^{-7}	mm
Geometric constant	α	0.45	–
Kinematic hardening	h	6555	MPa
Kinematic softening	h_D	245	–
Length-scale constant	C	10	–

in the RVE to avoid misrepresentation of a grain with a few number of elements. Similarly, the maximum limit (max. lim.) avoids the presence of very large grains that leads to under-representation of a polycrystal.

The effect of secondary phase delta-ferrite particles was neglected in this study. These second phases will give rise to local stress concentrations at the grain boundaries which act as potential sites for failure initiation (Sun et al., 2019a). However, the effect of delta-ferrite on the macroscopic stress of the electron beam welded SS316L was limited due to its low volume fraction (less than 1%), Fig. 1. Besides, the representatives of the polycrystal becomes computationally inefficient when the relatively small dimensions of the second-phase particles were considered. For these reasons, the delta-ferrite was not represented in the synthetic microstructures.

The uni-axial tensile test in the experiments was simulated by fixing the displacements that are normal to the three exterior surfaces. Uniform displacements to the nodes of one of the face of the RVE was employed as the tensile displacements. The simulations were performed up to 1.5% strain with a strain rate of 5×10^{-4} s^{-1}. Macroscopic stress in the simulations were computed by averaging the normal Cauchy (true) stress component along the loading direction amongst all of the elements in the mesh. The engineering strain was obtained by normalizing the displacements by the initial length of the RVE along loading direction which was later converted to true strain conventionally ($\epsilon_{true} = \ln(\epsilon_{eng} + 1)$).

4.1. Calibration (parent material)

Calibration was performed with respect to the mechanical response of the parent microstructure with homogeneous equiaxed grain structure and uniform crystallographic texture. The average microstructural response of the overall RVE was used for calibration with respect to the tensile experiments. A two stage calibration method was employed; at low strain and large strains to ensure the true behavior. Firstly, the calibration was performed up to 1.5% axial strain. Secondly, the fine tuning of the parameters was conducted using the experimental stress–strain curve up to 15% axial strain which was essential to ensure the matching strain hardening behavior.

The model calibration was accomplished iteratively by adjusting model parameters to match the experimental tensile test results for the parent material. Firstly, the yield strength was adjusted using the model constants of CRSS (τ_c^0) and statistically stored dislocation density (ϱ^0). Both parameters have the same effect on the yield strength, the latter effecting the strain hardening response

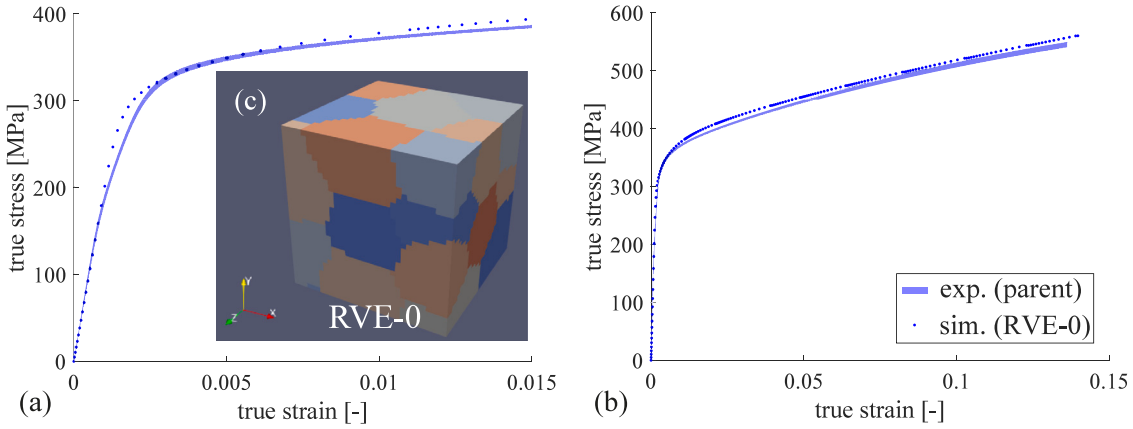

Fig. 9. Stress strain response for parent material, experiments (exp.) and simulations (sim.), after calibration up to the axial strains of (a) 1.5% and (b) 15% using (c) RVE-0 with a 32 × 32 × 32 grid. Loading was along x-direction.

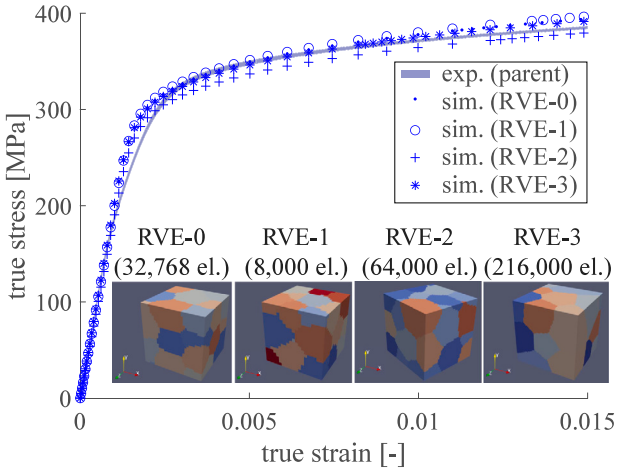

Fig. 10. Effect of RVE resolution (number of elements per grain) on the uni-axial stress–strain response; experiments (exp.) vs. simulations (sim.). Total number of elements are indicated in parentheses. RVE-0 refers to the reference RVE used for calibration. Loading was along x-axis.

as well. The initial value of CRSS shall not be confused with the lattice friction, rather it represents the initial strength of a slip system considering the overall effect of the microstructure, i.e. solid solution strengthening, hard obstacles, friction stress, etc. Secondly, the strain hardening rate was calibrated using the model constants K and y_c. Elastic modulus of austenite at the room temperature were used (Ledbetter, 1985). The reference slip rate and sensitivity exponent ($\dot{\gamma}_0$ and m) were assumed to be within the widely-accepted range of values of 0.001–0.1 s^{-1} and 0.001–0.5, respectively. The backstress parameters (h and h_D) were obtained from the Ref. Agius et al. (2020) that rely on the cyclic experimental response of a similar material (SS316H) which has a similar cyclic behavior as the material of interest (SS316L) at room temperature. Table 3 shows the final calibrated model parameters.

Fig. 9 shows the macroscopic tensile stresses obtained by experiments and its comparison to the results obtained after the calibration. The predicted and experimental curves were slightly different in the low strain regime up to 1.5% strain. The experiments show transition to non-linear regime after approximately 200 MPa. This could be related with the residual stresses present in the weldment. Calibration can be performed with better mesh refinement for accuracy but then it becomes extremely time consuming. Therefore, we used an inverse approach to check the representability of the RVE and validate the calibration by further investigating the sensitivity of stress–strain curve to the RVE resolution and RVE size.

4.2. RVE resolution (parent material)

The effect of RVE resolution was investigated by changing the voxel size while keeping the overall dimensions of the RVE and the grain size statistics constant. Therefore, in this analysis the number of grains within the RVEs remains nearly the same because grain size statistics are kept the same for all RVEs, Table 2. But the orientations were different due to random generation of microstructures everytime.

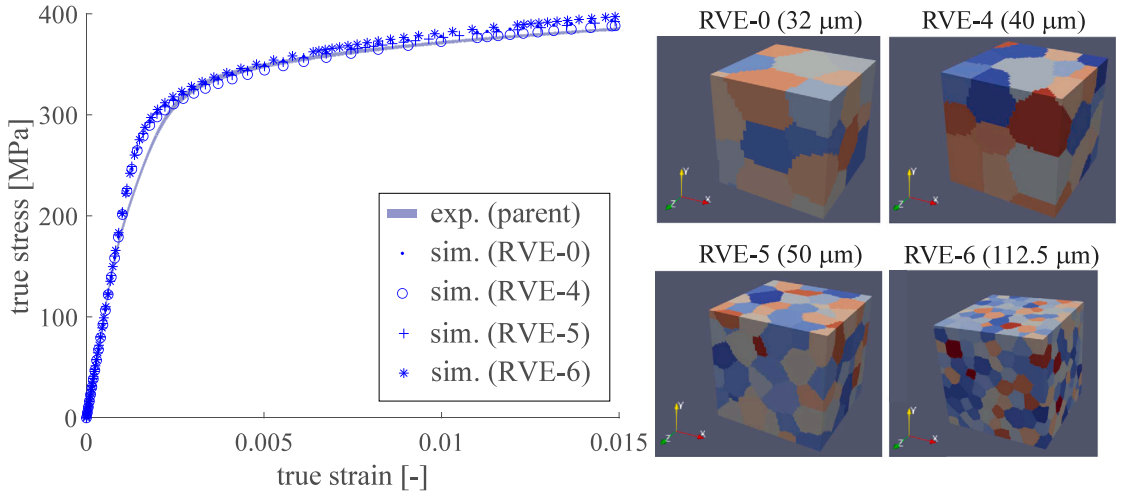

Fig. 11. Effect of RVE size (total number of grains) on uni-axial stress–strain response; experiments (exp.) vs. simulations (sim.). The edge length of each RVE is indicated in parentheses. Loading was along *x*-axis.

Fig. 10 shows the comparison of macroscopic stress–strain response of different RVEs. The difference between the flow stresses for case with the lowest resolution (RVE-2) and the highest resolution (RVE-3) is negligible at the considered low strain level. RVE-0, RVE-1, RVE-2, and RVE-3 have 1260, 320, 2462, and 8640 elements per grain on average, respectively. RVE-0 contains over a thousand elements per grain revealing a converged response. This value is consistent with the findings in the Ref. Lim et al. (2019), which gives approximately 1% variation among the results for RVE having less than 1000 elements per grain for the uni-axial strain of 1%. The scatter in the stress–strain curves is reasonable considering the randomly generated orientations for each RVE thereby leading to a different response.

4.3. RVE size (parent material)

Four different RVEs with different dimensions were examined in an effort to find the appropriate synthetic representation of a polycrystal. All four RVEs have the same grain size statistics and RVE resolution, Table 2. Therefore, RVE-4, RVE-5 and RVE-6 were obtained by simply increasing the dimensions by increasing the number of divisions while keeping the voxel size constant.

Fig. 11 shows the stress–strain response of RVEs with different sizes. RVE-0, RVE-4, RVE-5 and RVE-6 contain 26, 50, 156, and 517 total number of grains, respectively. The difference between using an RVE containing 26 grains and 517 grains was approximately only 5 MPa at 1.5% strain revealing RVE-0 being adequately representative of the parent material in the absence of morphological and crystallographic texture. Lim et al. (2019). A greater number of grains is expected to represent the weldment in the presence of crystallographic texture. However, the representatives also depends on the strain levels and low number of grains are representative of a textured polycrystal at low strains (<2%).

4.4. Crystallographic texture (weldment)

The crystallographic texture obtained from the EBSD measurements of the weld, Fig. 2(a), were incorporated to RVE-8/9 that represent the weld. The grains having dimensions greater than 100 μm were identified using MTEX® and exported as a text file input suitable for the synthetic microstructure generator, Dream3D® software. Fig. 12 shows the pole figures of the exported and imported grain orientations both having the same sample directions for consistency.

The crystallographic texture shall be considered in the weld models for accurate mechanical predictions. The elastic stiffness of RVE-7, without considering the crystallographic texture, was quite different than that of the weld. The presence of crystallographic texture in RVE-8 leads to a significantly better match with the weld response. Therefore, the lower elastic stiffness and the reduced yield stresses in the weld than the parent material is strongly linked with the presence of the crystallographic texture consisting of mainly Goss and Cube (rotated Cube) texture components, Fig. 12(a)–(b).

Morphological texture and grain size have a relatively lower effect on the mechanical response of the weld. This can be clearly concluded from the stress–strain response of RVE-7 which does not posses crystallographic texture but has large grains relative to the parent. However, the subtantial change in the grain size and morphology, did not significantly influence the yield response with respect to the parent material. It would appear that, the grain size and morphology have a secondary effect in comparison to the crystallographic texture at the considered scale of grain dimensions.

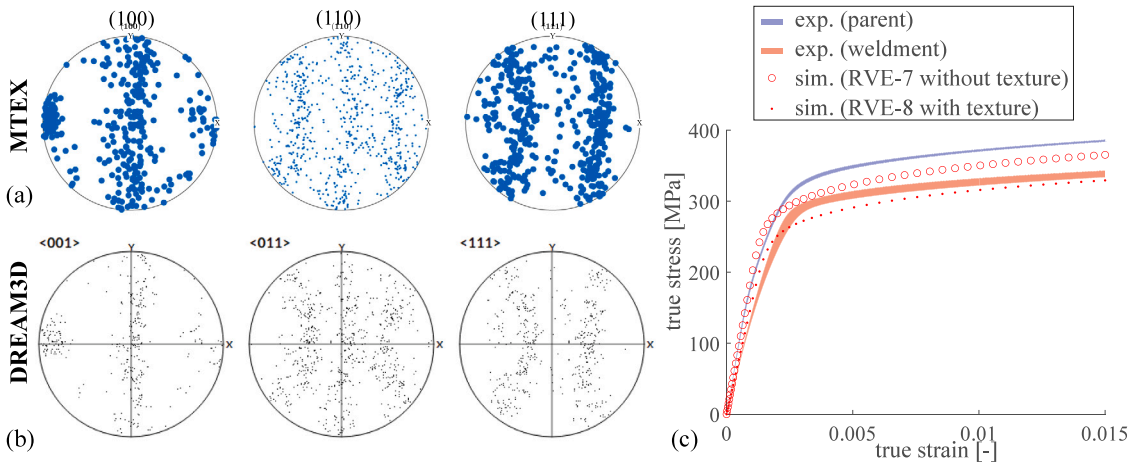

Fig. 12. (a) Experimental texture in MTEX® for grain with sizes larger than 100 μm, (b) imported texture pole figures in DREAM3D®, (c) uni-axial stress–strain curve of experiments (exp.) and simulations (sim.). Loading was along z-axis.

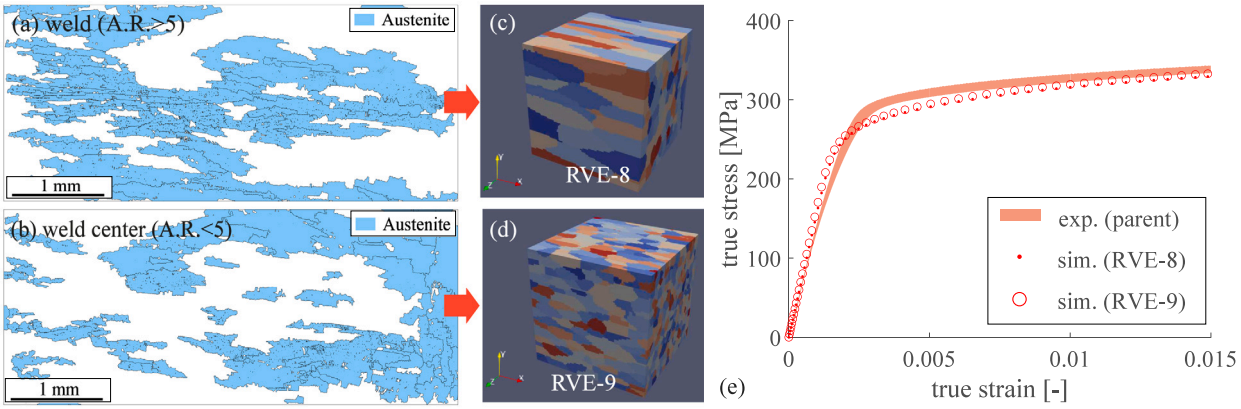

Fig. 13. The effect of grain aspect ratio on the uni-axial stress–strain response for weldment. The highlighted regions in blue color on the EBSD map shows (a) grains AR > 5, (b) grains with AR < 5. Synthetic RVEs generated using the two different grain size statistics obtained from the EBSD map including the crystallographic texture; (c) RVE-8, (d) RVE-9. Corresponding (e) experimental (exp.) and simulated (sim.) stress–strain curves for the weldment. Loading was along z-axis.

4.5. Grain aspect ratio (weldment)

Fig. 13 shows the comparison of different grain families with different aspect ratios. RVE-8 and RVE-9 well represent the mechanical behavior of the weld. Although we used aspect ratios to differentiate different grain families, the selection of grains with two different aspect ratios indeed also reveals different average grain sizes. Comparison of stress–strain response of RVE-8 and RVE-9 with different grain sizes reveals the relatively weak effect of the grain size at this scale, Fig. 8. The slight increase in the flow stress of as the average grain size decreases (RVE-8 with respect to RVE-9) is consistent with Hall–Petch type models. The mechanical behavior at considered scale is mainly governed by the crystallographic texture. Similarly, the difference in the grain size and morphology has a secondary effect which can also be concluded by comparing the stress–strain curves for RVE-8 and RVE-9, Fig. 13.

4.6. Prior strains due to welding process

The lower yield stress and higher strain hardening predicted by the weld material simulations than that of the experiments can be a consequence of pre-strains which take place during the welding process. Weld pre-strain history has not been included in the simulations meaning that the material was treated undeformed without any prior strain in the simulations. Ignoring the effect of prestrain has led to an approximate 7% mismatch in the predicted flow stress. The difference in the strain hardening rate is greater; approximately 3489 MPa in the experiments while it is 2567 MPa for RVE-8, which makes 26% mismatch of approximately, Fig. 13.

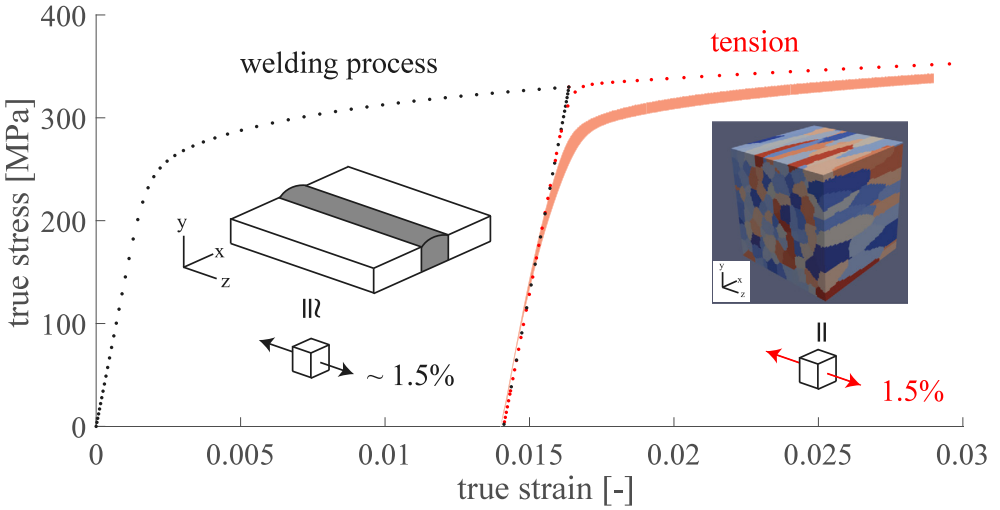

Fig. 14. Stress–strain curves of the approximated welding process (black dots) followed by tensile testing (red dots).

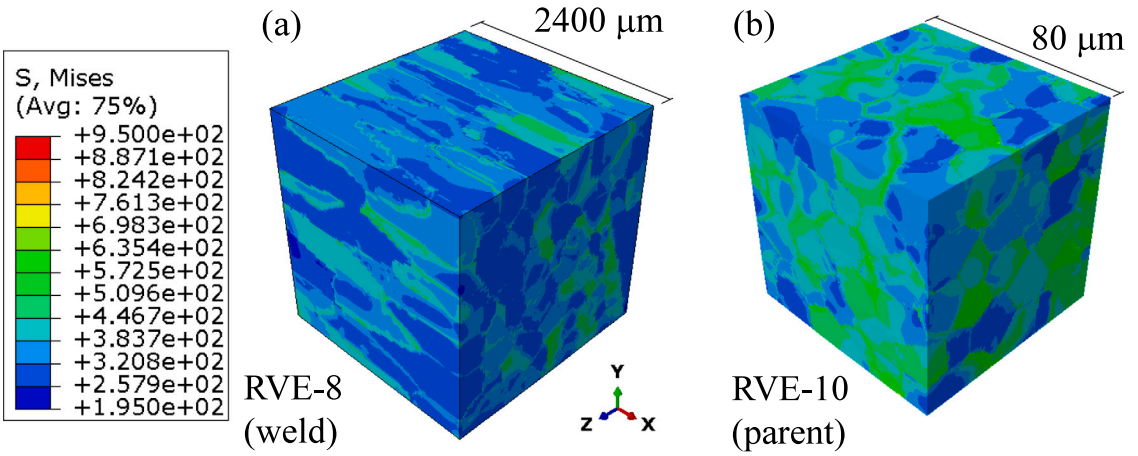

Fig. 15. Equivalent Von Mises stress distributions on (a) RVE-8 (weld) and (b) RVE-10 (parent) after loading up to 1.5% strain. Loading is along z and x directions for RVE-8 and RVE-10, respectively.

To further investigate the effect weld process strains, the weldment was preloaded up to 1.5% pre-strain, which is the expected strain tensile strain level after welding along longitudinal or welding direction (z-axis) (Smith and Smith, 2018), and then the loading was released. After the application of this pre-strain, the tensile experiments on the weld was simulated for RVE-8, Fig. 14 in the same way as described previously. The simulation of the weld process strains by this approximation revealed over prediction of the yield strength and under prediction of the strain hardening in comparison to the experiments.

The mismatch in the simulated flow stresses and the experimental stress could be due to various reasons: **i.** The process strains are far more complicated than uni-axial strain state. Shear strains can be ignored at the centerline of the weld, however, the presence of the normal strain components along the transverse directions (x and y directions) cannot be neglected. In addition, the strains during welding change their sign upon cooling. **ii.** The strain rate is expected to be different in welding than the uni-axial tests with 5×10^{-4} s^{-1}. **iii.** The presence of residual stresses may be reason in the decreased flow stresses measured in the experiments. **iv.** Neglecting the high temperatures and temperature dependent material properties; lower elasticity and lower yield stress, during welding also leads to the overestimation of flow stress in the simulations. **v.** The stress relaxation effects during welding were also neglected that would lower the flow stresses. Therefore, the simulation of welding process requires temperature dependent material properties and coupling with welding process simulations to accurately predict the weldment response by incorporating process strains, strain-rates, temperatures and stress relaxation effects to the model.

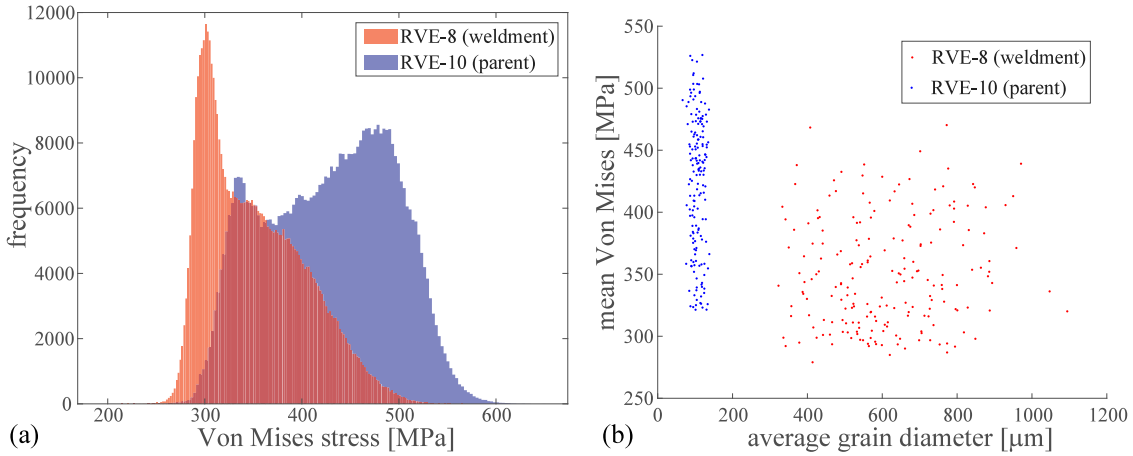

Fig. 16. Von Mises stress: (a) frequency distribution over the RVE, (b) mean value over each grain vs. average grain diameter. The dark region indicates the intersection of the two distributions.

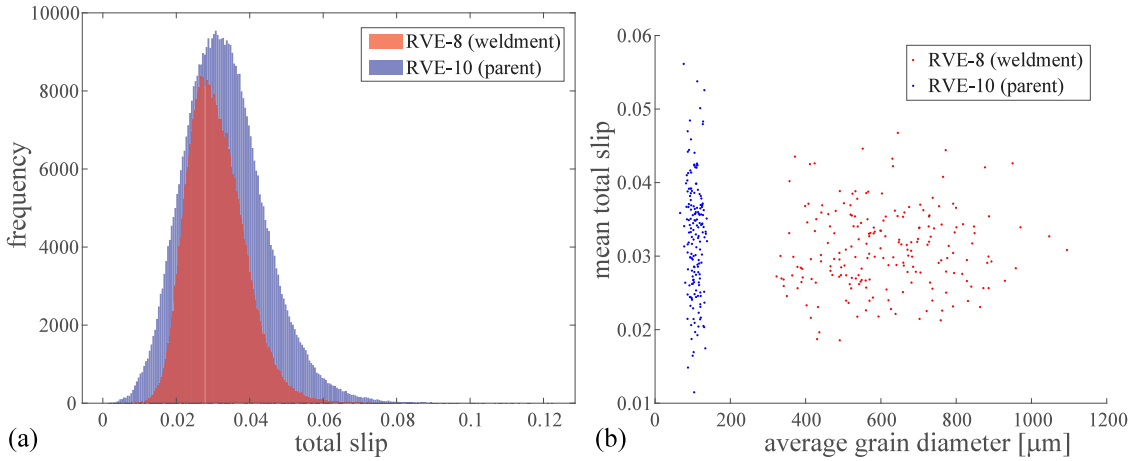

Fig. 17. Cumulative slip, Γ: (a) frequency distribution over the RVE, (b) mean value over each grain vs. grain average diameter. The dark region indicates the intersection of the two distributions.

4.7. Parent vs. weldment

Von Mises stress distributions of parent and weldment after 1.5% tensile strain and unloading reveal a quantitatively higher stress levels in the parent than the weldment, Fig. 15. However, large stresses are also present in the weldments. The stress gradients at the grain boundary interfaces were larger for the weldment than the parent material thereby making weldment more prone to failure.

Fig. 16 shows a comparison of Von Mises stresses averaged over each grain of the weld (RVE-8) and parent (RVE-10) microstructures. The mean Von Mises stress in the parent material (428.1 MPa) is higher than that of the weld (351.6 MPa), Fig. 16(a). The mean Von-Mises stress distribution in the parent material has a wider range with respect to the weld with the standard deviations of 66.1 MPa and 51.8 MPa, respectively, Fig. 16(b), that indicates a greater local variation of stresses within the grains of parent material.

Similarly, average cumulative slip amongst the grains was investigated for the parent and weldment. The frequency plots in Fig. 17(a) show a wider range of values for parent material indicating a greater variation of slip amongst grains of the parent material than the weldment. The crystallographic texture in the weldment has 43.6% less variation in mean cumulative slip relative to the parent material. The mean value of the cumulative slip in Fig. 17(b) has a wider range of values than the parent material due to the presence of relatively random crystal orientations of parent grains in comparison to the sharp texture in the weldment.

In summary the grain-size dependent model was implemented in a modular crystal plasticity framework to simulate the polycrystal mechanical response accurately and efficiently. The model reveals a higher yield stress for smaller grains without any prior slip which is the major difference from the strain gradient models. The model requiring only a few parameters for calibration makes it quite efficient. However the calibration of length-scale adjusting parameter, C, needs further investigation including experiments on polycrystals with a range of average grain sizes. The model is computationally efficient since it does not require a

non-local calculation and the related calculations need to be performed only once at the beginning of the analysis. Therefore, the computational times were approximately the same as using a size-independent model, making this model extremely efficient. Besides, the size dependent model increases the CRSS based on the projected grain size on the slip distance having a different influence on slip systems. Increasing the CRSS, is seen to improve the convergence revealing the robustness of the proposed length-scale model for polycrystals. To conclude, the model presents a robust and numerically efficient alternative method to incorporate size dependence for large scale polycrystal applications.

5. Conclusions

This study presents a relatively straightforward and consistent way to incorporate grain size and shape dependence to the crystal plasticity based finite element methods. Several important conclusions are listed in the below:

- The effect of grain size and morphology on the yield strength and strain hardening rate were successfully included by representation of grains with ellipsoids and considering the effect of grain shape on the mean-free-path of dislocations.
- The proposed length-scale model changes both the yield strength and strain hardening as a function of grain size unlike strain gradient methods that cause strengthening by strain hardening.
- The observed grain size dependence is low but still present for the size regime considered in this study.
- Crystallographic texture is the most important factor to accurately model mechanical response of electron-beam welded material microstructure and must be included the models.
- At the low strain levels (1.5% axial strain), the RVE becomes statistically representative of a polycrystal as the number of elements per grain becomes more than 1000 and total number of grains becomes more than 25 number of grains for an equiaxed microstructure without texture.

Future studies include a more detailed microstructural characterization of the weld using 3D-EBSD technique over a large region to have a more accurate representation of crystallographic texture. Furthermore, the proposed crystal plasticity approach will be coupled to the weld process simulations to incorporate the effect of strain history of the weldment prior to the tensile simulations.

Declaration of competing interest

The authors declare that they have no known competing financial interests or personal relationships that could have appeared to influence the work reported in this paper.

Data availability

The shared folder contains a working version of the UMAT code (BRISTOL), ABAQUS environment files, a user guide, and example files that was developed within this study.

Acknowledgments

Authors acknowledge funding support from the Synergistic utilization of Informatics and Data centRic Integrity engineering (SINDRI) project that is funded by Engineering and Physical Sciences Research Council (EPSRC) of UK through contract no. EP/V038079/1 and EP/R020108/1 and EDF Energy. Production of the weldment at the Nuclear Advanced Manufacturing Research Centre (NAMRC) was supported by UK's Department of Business, Energy and Industrial Strategy Nuclear Innovation Programme and was conducted and managed by Frazer-Nash Consultancy. The views expressed in the paper are those of the authors and should not be interpreted as BEIS or wider Government policy. We also greatly appreciate the personal communication with Prof. P.R. Dawson and his invaluable comments on the representation of polycrystals.

Appendix A. Crystal orientation

Crystal orientation matrix, **g**, defines the passive transformation from the sample to the crystal reference frame, Eq. (A.1). **g** is computed by Bunge angles $(\varphi_1, \Phi, \varphi_2)$.

$$\mathbf{g} = \begin{bmatrix} \cos\varphi_1 \cos\varphi_2 - \sin\varphi_1 \sin\varphi_2 \cos\Phi & \sin\varphi_1 \cos\varphi_2 - \cos\varphi_1 \sin\varphi_2 \cos\Phi & \sin\varphi_2 \sin\Phi \\ -\cos\varphi_1 \sin\varphi_2 - \sin\varphi_1 \cos\varphi_2 \cos\Phi & -\sin\varphi_1 \sin\varphi_2 + \cos\varphi_1 \cos\varphi_2 \cos\Phi & \cos\varphi_2 \sin\Phi \\ \sin\varphi_1 \sin\Phi & -\cos\varphi_1 \sin\Phi & \cos\Phi \end{bmatrix}. \tag{A.1}$$

Appendix B. Crystal orientations as initial rotations

The crystal orientations are assigned as initial plastic part of the deformation gradient, $\mathbf{F^p}_{t0}$ (Ma, 2006). Eq. (B.1) allows direct transformation of a vector in the sample reference to crystal reference thereby eliminating the need for transformation of elasticity and slip vectors:

$$\mathbf{F^p}_{t0} = \mathbf{g}. \tag{B.1}$$

The transpose (inverse) of the crystal orientation is assigned as the initial (at $t = 0$ s) elastic deformation gradient, $\mathbf{F^e}_{t0}$, using Eq. (B.2):

$$\mathbf{F^e}_{t0} = \mathbf{g}^T. \tag{B.2}$$

So that, there is no initial deformation, Eq. (B.3):

$$\mathbf{F}_{t0} = \mathbf{F^e}_{t0}\,\mathbf{F^p}_{t0} = \mathbf{I}. \tag{B.3}$$

Appendix C. Crystal plasticity time integration scheme

Time integration of evolution of $\mathbf{F^p}$ gives approximately the expression in Eq. (C.1) in terms of the plastic velocity gradient, $\mathbf{L^p}$, and plastic deformation gradient at the former time step, $\mathbf{F^p}_t$:

$$\mathbf{L^p} = \frac{\mathbf{F^p} - \mathbf{F^p}_t}{\Delta t}\,\mathbf{F^{p-1}}. \tag{C.1}$$

Rearranging terms in Eq. (C.1) and using Eq. (6) gives Eq. (C.2):

$$\mathbf{F^{p-1}} = \mathbf{F^{p-1}_t}\left(\mathbf{I} - \sum_a \mathbf{S}^a \Delta\gamma^a\right). \tag{C.2}$$

Using Eq. (1) and Green–Lagrange expression in Eq. (2) reveals elastic strains in terms of the plastic part of the deformation gradient, Eq. (C.3):

$$\mathbf{P} = \mathbf{D} : \left(\mathbf{F^{p-T}}\,\mathbf{F}^T\,\mathbf{F}\,\mathbf{F^{p-1}} - \mathbf{I}\right)/2. \tag{C.3}$$

Substituting Eq. (C.2) into Eq. (C.3) and neglecting higher order shear terms gives the relation of 2nd PK stress in which $\mathbf{P}^{tr}$ is the trial stress and a plastic corrector term, Eq. (C.4):

$$\mathbf{P} = \mathbf{P}^{tr} - \sum_a \Delta\gamma^a\,\mathbf{C}^a. \tag{C.4}$$

in which $\mathbf{P}^{tr}$ is given by Eq. (C.5):

$$\mathbf{P}^{tr} = \mathbf{D} : (\mathbf{A} - \mathbf{I})/2. \tag{C.5}$$

$\mathbf{C}^a$ is defined by Eq. (C.6):

$$\mathbf{C}^a = \mathbf{D} : \mathbf{B}^a/2. \tag{C.6}$$

$\mathbf{A}$ is computed from the given quantities using Eq. (C.7):

$$\mathbf{A} = \mathbf{F^{p-T}_t}\,\mathbf{F}^T\,\mathbf{F}\,\mathbf{F^{p-1}_t}. \tag{C.7}$$

$\mathbf{B}^a$ is computed from Eq. (C.8) which reads:

$$\mathbf{B}^a = \mathbf{A}\,\mathbf{S}^a + (\mathbf{S}^a)^T\,\mathbf{A}. \tag{C.8}$$

The residual in Eq. (C.9) is formulated and its iterative solution is performed by using a two level scheme:

$$\boldsymbol{\Psi} = \mathbf{P} - \mathbf{P}^{tr} + \sum_a \Delta\gamma^a\,\mathbf{C}^a. \tag{C.9}$$

In the inner level Eq. (C.9) is solved by Newton–Raphson method using the tangent in Eq. (C.10). The derivative expression, $\frac{\partial\dot{\gamma}^a}{\partial\tau^a}$, in the tangent calculation is obtained by the constitutive coupling:

$$\frac{\partial\boldsymbol{\Psi}}{\partial\mathbf{P}} = \mathbf{I} + \sum_a \frac{\partial\dot{\gamma}^a}{\partial\tau^a}\,\mathbf{S}^a\,\Delta t. \tag{C.10}$$

The updated value of stresses at the next inner iteration cycle, $(i+1)$, are obtained by Eq. (C.11). The iteration continues until the residual becomes smaller than a tolerance ($\|\boldsymbol{\Psi}\| < 10^{-6} \times \tau_c^0$):

$$\mathbf{P}_{(i+1)} = \mathbf{P}_{(i)} - \left(\frac{\partial\boldsymbol{\Psi}}{\partial\mathbf{P}}\right)^{-1}_{(i)} \boldsymbol{\Psi}_{(i)}. \tag{C.11}$$

Once the inner level converges, the converged slip rates are used in conjunction with the constitutive relations in Eqs. (11) and (12) to update the corresponding state variables using Euler integration. In this study, dislocation density and backstress were used as the state variables. However, to keep the generality, Eq. (C.12) exemplifies a generalized state update in which $[Y^a_{(j+1)}]_n$ and $[Y^a_{(j)}]_n$ represent current and former values of the states per slip system a at the "j"th outer level iteration. The subscript n represents the number of independent state variables. The outer level iteration continues until the residual for each state variables becomes smaller than a tolerance ($|\,[\dot{Y}^a_{(j)}]_n\,\Delta t\,| < 10^{-5} \times Y^0_n$):

$$\left[Y^a_{(j+1)}\right]_n = \left[\dot{Y}^a_{(j)}\right]_n \Delta t + \left[Y^a_{(j)}\right]_n. \tag{C.12}$$

Single level iterative schemes as suggested by Meissonnier et al. was also tested using a material point application of crystal plasticity solver. However, it did not provide a significant saving in the computation times as per suggested in the Meissonnier et al. (2001) and Ha et al. (2017).

Appendix D. Analytical material tangent calculation

Material tangent in ABAQUS® uses the engineering strains, $\boldsymbol{\epsilon}$, and Cauchy stress components, $\boldsymbol{\sigma}$, Eq. (D.1):

$$\boldsymbol{\epsilon} = \begin{bmatrix} \epsilon_{xx} \\ \epsilon_{yy} \\ \epsilon_{zz} \\ 2\epsilon_{xy} \\ 2\epsilon_{xz} \\ 2\epsilon_{yz} \end{bmatrix}, \quad \boldsymbol{\sigma} = \begin{bmatrix} \sigma_{xx} \\ \sigma_{yy} \\ \sigma_{zz} \\ \sigma_{xy} \\ \sigma_{xz} \\ \sigma_{yz} \end{bmatrix}. \tag{D.1}$$

The fourth order Jacobian or the material tangent tensor, $\mathbf{J}$, is given by Eq. (D.2):

$$\partial\boldsymbol{\sigma} = \mathbf{J} : \partial\boldsymbol{\Delta}\mathbf{E}. \tag{D.2}$$

The variation of Cauchy stress is computed by differentiating the expression for Cauchy stress in Eq. (7) to obtain Eq. (D.3):

$$\partial\boldsymbol{\sigma} = \frac{1}{\det\mathbf{F^e}}\left[\partial\mathbf{F^e}\,\mathbf{P}\,\mathbf{F^{e}}^T + \mathbf{F^e}\,\partial\mathbf{P}\,\mathbf{F^{e}}^T + \mathbf{F^e}\,\mathbf{P}\,\partial\mathbf{F^{e}}^T - \mathbf{F^e}\,\mathbf{P}\,\mathbf{F^{e}}^T\,\partial\mathbf{F^e} : \mathbf{F^{e}}^{-T}\right]. \tag{D.3}$$

The relative strain, $\boldsymbol{\Delta}\mathbf{E}$, is obtained from the relative stretch, $\boldsymbol{\Delta}\mathbf{U}$, using Eq. (D.4):

$$\boldsymbol{\Delta}\mathbf{E} = \ln(\boldsymbol{\Delta}\mathbf{U}) \approx \boldsymbol{\Delta}\mathbf{U} - \mathbf{1}. \tag{D.4}$$

The variation of relative strains becomes as in Eq. (D.5):

$$\partial\boldsymbol{\Delta}\mathbf{E} = \partial\boldsymbol{\Delta}\mathbf{U}. \tag{D.5}$$

The relative stretch is computed first by obtaining the relative deformation gradient, $\boldsymbol{\Delta}\mathbf{F}$, from the total deformation gradients at the current and former time steps using Eq. (D.6):

$$\boldsymbol{\Delta}\mathbf{F} = \mathbf{F}\,\mathbf{F}_t^{-1}. \tag{D.6}$$

The polar decomposition of the relative deformation gradient, $\boldsymbol{\Delta}\mathbf{F}$, is used to give the relative stretch, $\boldsymbol{\Delta}\mathbf{U}$, and relative rotation, $\boldsymbol{\Delta}\mathbf{R}$.

(i) Calculation of $\dfrac{\partial\mathbf{F^e}}{\partial\boldsymbol{\Delta}\mathbf{U}}$

Elastic part of the deformation gradient can be written as in Eq. (D.7) using Eqs. (1) and (C.2):

$$\mathbf{F^e} = \boldsymbol{\Delta}\mathbf{R}\,\boldsymbol{\Delta}\mathbf{U}\,\mathbf{F^e}_t\left(1 - \sum_a \Delta\gamma^a\,\mathbf{S}^a\right). \tag{D.7}$$

Differentiation reveals Eq. (D.8):

$$\partial\mathbf{F^e} = \boldsymbol{\Delta}\mathbf{R}\,\partial\boldsymbol{\Delta}\mathbf{U}\,\mathbf{F^e}_t\left(1 - \sum_a \Delta\gamma^a\,\mathbf{S}^a\right) - \boldsymbol{\Delta}\mathbf{R}\,\boldsymbol{\Delta}\mathbf{U}\,\mathbf{F^e}_t\sum_a \partial\Delta\gamma^a\,\mathbf{S}^a. \tag{D.8}$$

(ii) Calculation of $\dfrac{\partial\Delta\gamma^a}{\partial\boldsymbol{\Delta}\mathbf{U}}$

Using chain rule of differentiation Eq. (D.9) is calculated:

$$\frac{\partial\Delta\gamma^a}{\partial\boldsymbol{\Delta}\mathbf{U}} = \frac{\partial\Delta\gamma^a}{\partial\mathbf{P}}\,\frac{\partial\mathbf{P}}{\partial\boldsymbol{\Delta}\mathbf{U}}. \tag{D.9}$$

(iii) Calculation of $\dfrac{\partial\Delta\gamma^a}{\partial\mathbf{P}}$

Using chain rule Eq. (D.10) can be obtained in which the term $\dfrac{\partial\Delta\gamma^a}{\partial\tau^a}$ is obtained by the constitutive law:

$$\frac{\partial\Delta\gamma^a}{\partial\mathbf{P}} = \frac{\partial\Delta\gamma^a}{\partial\tau^a}\,\frac{\partial\tau^a}{\partial\mathbf{P}}. \tag{D.10}$$

Resolved shear stress is related 2nd PK stress through Eq. (4) which takes the form in Eq. (D.11) after differentiation:

$$\frac{\partial \tau^a}{\partial \mathbf{P}} = \frac{1}{2}\left[\mathbf{S}^a + (\mathbf{S}^a)^T\right]. \tag{D.11}$$

(iv) Calculation of $\frac{\partial \mathbf{P}}{\partial \Delta \mathbf{U}}$

Differentiating Eq. (C.4), gives two other differentials to be computed as in Eq. (D.12):

$$\partial \mathbf{P} = \partial \mathbf{P}^{tr} - \sum_a \partial \Delta\gamma^a \, \mathbf{C}^a - \sum_a \Delta\gamma^a \, \partial \mathbf{C}^a. \tag{D.12}$$

(v) Calculation of $\frac{\partial \mathbf{C}^a}{\partial \Delta \mathbf{U}}$

Taking derivative of the expression in Eq. (C.6) gives Eq. (D.13):

$$\partial \mathbf{C}^a = \frac{1}{2}\mathbf{D} : \partial \mathbf{B}^a. \tag{D.13}$$

(vi) Calculation of $\frac{\partial \mathbf{B}^a}{\partial \Delta \mathbf{U}}$

The expression for $\mathbf{B}^a$ in Eq. (C.8) is differentiated as in Eq. (D.14):

$$\partial \mathbf{B}^a = \partial \mathbf{A} \, \mathbf{S}^a + (\mathbf{S}^a)^T \, \partial \mathbf{A}. \tag{D.14}$$

(vii) Calculation of $\frac{\partial \mathbf{P}^{tr}}{\partial \Delta \mathbf{U}}$

Using chain rule and differentiating Eq. (C.5), the derivative of trial stress is obtained, Eq. (D.15):

$$\partial \mathbf{P}^{tr} = \frac{1}{2}\mathbf{D} : \partial \mathbf{A}. \tag{D.15}$$

(viii) Calculation of $\frac{\partial \mathbf{A}}{\partial \Delta \mathbf{U}}$

$\partial \mathbf{A}$ is necessary for calculation of differentials in both Eqs. (D.14) and (D.15). The derivative of the expression for $\mathbf{A}$ in Eq. (C.7) is used together with Eqs. (1) and (D.6) to give Eq. (D.16):

$$\partial \mathbf{A} = \mathbf{F}^{\mathbf{e}T}_t \, \partial \Delta\mathbf{U} \, \Delta\mathbf{U} \, \mathbf{F}^{\mathbf{e}}_t + \mathbf{F}^{\mathbf{e}T}_t \, \Delta\mathbf{U} \, \partial \Delta\mathbf{U} \, \mathbf{F}^{\mathbf{e}}_t. \tag{D.16}$$

Once these differentials in steps (i)–(viii) are completed, the Jacobian is calculated using Eq. (D.3). The index notation is not shown here to avoid complexity, readers shall refer to the Dai (1997) and Balasubramanian (1995) for further details.

The assignment of crystal orientations to the initial plastic deformation gradient (Eq. (B.2)) and its inverse to the elastic deformation gradient (Eq. (B.3)) eliminates the transformation of cubic elasticity (Step-2 in Balasubramanian, 1995) as well as the transformation of slip vectors and Schmid tensor.

Appendix E. Supplementary data

Supplementary material related to this article can be found online at https://doi.org/10.1016/j.jmps.2023.105331.

References

Acharya, A., Roy, A., 2006. Size effects and idealized dislocation microstructure at small scales: predictions of a phenomenological model of mesoscopic field dislocation mechanics: Part I. J. Mech. Phys. Solids 54 (8), 1687–1710.

Agius, D., Al Mamun, A., Simpson, C.A., Truman, C., Wang, Y., Mostafavi, M., Knowles, D., 2020. Microstructure-informed, predictive crystal plasticity finite element model of fatigue-dwells. Comput. Mater. Sci. 183, 109823.

Agius, D., Kareer, A., Al Mamun, A., Truman, C., Collins, D.M., Mostafavi, M., Knowles, D., 2022. A crystal plasticity model that accounts for grain size effects and slip system interactions on the deformation of austenitic stainless steels. Int. J. Plast. 152, 103249.

Ardeljan, M., Beyerlein, I.J., Knezevic, M., 2014. A dislocation density based crystal plasticity finite element model: Application to a two-phase polycrystalline HCP/BCC composites. J. Mech. Phys. Solids 66, 16–31.

Arora, R., Acharya, A., 2020. A unification of finite deformation J2 Von-Mises plasticity and quantitative dislocation mechanics. J. Mech. Phys. Solids 143, 104050.

Arsenlis, A., Parks, D.M., 2002. Modeling the evolution of crystallographic dislocation density in crystal plasticity. J. Mech. Phys. Solids 50 (9), 1979–2009.

ASTM-E112-13, 2017. Standard test methods for determining average grain size. In: Annual Book of ASTM Standards. American Society for Testing and Materials, West Conshohocken.

ASTM-E8, 2001. Standard test methods for tension testing of metallic materials. In: Annual Book of ASTM Standards. ASTM.

Balasubramanian, S., 1995. Polycrystalline Plasticity and its Applications to Deformation Processing (Ph.D. thesis). Massachusetts Institute of Technology.

Barton, N.R., Arsenlis, A., Marian, J., 2013. A polycrystal plasticity model of strain localization in irradiated iron. J. Mech. Phys. Solids 61 (2), 341–351.

Chen, J., Wang, Z., Korsunsky, A.M., 2022. Multiscale stress and strain statistics in the deformation of polycrystalline alloys. Int. J. Plast. 152, 103260.

Cheong, K., Busso, E., Arsenlis, A., 2005. A study of microstructural length scale effects on the behaviour of FCC polycrystals using strain gradient concepts. Int. J. Plast. 21 (9), 1797–1814.

Chowdhury, S., Yadaiah, N., Khan, S.M., Ozah, R., Das, B., Muralidhar, M., 2018. A perspective review on experimental investigation and numerical modeling of electron beam welding process. Mater. Today: Proc. 5 (2), 4811–4817.

Cruzado, A., Lucarini, S., LLorca, J., Segurado, J., 2018. Crystal plasticity simulation of the effect of grain size on the fatigue behavior of polycrystalline Inconel 718. Int. J. Fatigue 113, 236–245.

Dai, H., 1997. Geometrically-Necessary Dislocation Density in Continuum Plasticity Theory, FEM Implementation and Applications (Ph.D. thesis). Massachusetts Institute of Technology.
Das, K., Ghosh, A., Bhattacharya, A., Lanjewar, H., Majumdar, J.D., Ghosh, M., 2021. Effect of beam current on the microstructure, crystallographic texture and mechanical properties of electron beam welded high purity niobium. Mater. Charact. 179, 111318.
Demir, E., Gutierrez-Urrutia, I., 2021. Investigation of strain hardening near grain boundaries of an aluminum oligocrystal: experiments and crystal based finite element method. Int. J. Plast. 136, 102898.
Evers, L., Brekelmans, W., Geers, M., 2004. Non-local crystal plasticity model with intrinsic SSD and GND effects. J. Mech. Phys. Solids 52 (10), 2379–2401.
Fleck, N., Hutchinson, J., 2001. A reformulation of strain gradient plasticity. J. Mech. Phys. Solids 49 (10), 2245–2271.
Fleck, N., Muller, G., Ashby, M.F., Hutchinson, J.W., 1994. Strain gradient plasticity: theory and experiment. Acta Metall. Mater. 42 (2), 475–487.
Gerken, J.M., Dawson, P.R., 2008. A crystal plasticity model that incorporates stresses and strains due to slip gradients. J. Mech. Phys. Solids 56 (4), 1651–1672.
Groeber, M.A., Jackson, M.A., 2014. DREAM. 3D: a digital representation environment for the analysis of microstructure in 3D. Integr. Mater. Manuf. Innov. 3 (1), 56–72.
Gurtin, M.E., 2002. A gradient theory of single-crystal viscoplasticity that accounts for geometrically necessary dislocations. J. Mech. Phys. Solids 50 (1), 5–32.
Ha, S., Jang, J.-H., Kim, K., 2017. Finite element implementation of dislocation-density-based crystal plasticity model and its application to pure aluminum crystalline materials. Int. J. Mech. Sci. 120, 249–262.
Hall, E.O., 1954. Variation of hardness of metals with grain size. Nature 173 (4411), 948–949.
Hansen, N., 2004. Hall–Petch relation and boundary strengthening. Scr. Mater. 51 (8), 801–806.
Haouala, S., Segurado, J., LLorca, J., 2018. An analysis of the influence of grain size on the strength of FCC polycrystals by means of computational homogenization. Acta Mater. 148, 72–85.
Hibbitt, D., Karlsson, B., Sorensen, P., 2014. ABAQUS User-Manual Release 6.14. Dassault Systèmes Simulia Corp., Providence, RI.
Huang, Y., 1991. A User-Material Subroutine Incroporating Single Crystal Plasticity in the ABAQUS Finite Element Program. Harvard Univ., Cambridge, MA.
Hutchinson, J.W., 2000. Plasticity at the micron scale. Int. J. Solids Struct. 37 (1–2), 225–238.
Kalidindi, S.R., Bronkhorst, C.A., Anand, L., 1992. Crystallographic texture evolution in bulk deformation processing of FCC metals. J. Mech. Phys. Solids 40 (3), 537–569.
Kapoor, K., Yoo, Y.S.J., Book, T.A., Kacher, J.P., Sangid, M.D., 2018. Incorporating grain-level residual stresses and validating a crystal plasticity model of a two-phase Ti-6Al-4 V alloy produced via additive manufacturing. J. Mech. Phys. Solids 121, 447–462.
Karapiperis, K., Stainier, L., Ortiz, M., Andrade, J., 2021. Data-driven multiscale modeling in mechanics. J. Mech. Phys. Solids 147, 104239.
Klusemann, B., Yalçinkaya, T., 2013. Plastic deformation induced microstructure evolution through gradient enhanced crystal plasticity based on a non-convex Helmholtz energy. Int. J. Plast. 48, 168–188.
Kocks, U., Mecking, H., 2003. Physics and phenomenology of strain hardening: the FCC case. Prog. Mater. Sci. 48 (3), 171–273.
Ledbetter, H., 1985. Predicted monocrystal elastic constants of 304-type stainless steel. Physica B+ C 128 (1), 1–4.
Liang, H., Dunne, F., 2009. GND accumulation in bi-crystal deformation: Crystal plasticity analysis and comparison with experiments. Int. J. Mech. Sci. 51 (4), 326–333.
Lieou, C.K., Bronkhorst, C.A., 2020. Thermodynamic theory of crystal plasticity: formulation and application to polycrystal fcc copper. J. Mech. Phys. Solids 138, 103905.
Lim, H., Battaile, C.C., Bishop, J.E., Foulk III, J.W., 2019. Investigating mesh sensitivity and polycrystalline RVEs in crystal plasticity finite element simulations. Int. J. Plast. 121, 101–115.
Liu, W., Lian, J., Aravas, N., Münstermann, S., 2020. A strategy for synthetic microstructure generation and crystal plasticity parameter calibration of fine-grain-structured dual-phase steel. Int. J. Plast. 126, 102614.
Lu, X., Dunne, F.P., Xu, Y., 2020. A crystal plasticity investigation of slip system interaction, GND density and stored energy in non-proportional fatigue in Nickel-based superalloy. Int. J. Fatigue 139, 105782.
Ma, A., 2006. Modeling the Constitutive Behavior of Polycrystalline Metals Based on Dislocation Mechanisms (Ph.D. Thesis). RWTH Aachen University, Aachen, Germany.
Mecking, H., Kocks, U., 1981. Kinetics of flow and strain-hardening. Acta Metall. 29 (11), 1865–1875.
Meissonnier, F., Busso, E., O'Dowd, N., 2001. Finite element implementation of a generalised non-local rate-dependent crystallographic formulation for finite strains. Int. J. Plast. 17 (4), 601–640.
Mokhtarishirazabad, M., Simpson, C., Horne, G., Kabra, S., Truman, C., Moffat, A., Mostafavi, M., 2019. Study of the fracture toughness in electron beam welds. In: Pressure Vessels and Piping Conference, Vol. 58974. American Society of Mechanical Engineers, V06AT06A053.
Mu, S., Tang, F., Gottstein, G., 2014. A cluster-type grain interaction deformation texture model accounting for twinning-induced texture and strain-hardening evolution: Application to magnesium alloys. Acta Mater. 68, 310–324.
Niordson, C.F., Kysar, J.W., 2014. Computational strain gradient crystal plasticity. J. Mech. Phys. Solids 62, 31–47.
Quey, R., Dawson, P., Barbe, F., 2011. Large-scale 3D random polycrystals for the finite element method: Generation, meshing and remeshing. Comput. Methods Appl. Mech. Engrg. 200 (17–20), 1729–1745.
Roters, F., Raabe, D., Gottstein, G., 2000. Work hardening in heterogeneous alloys—a microstructural approach based on three internal state variables. Acta Mater. 48 (17), 4181–4189.
Smith, M.C., Smith, A.C., 2018. Advances in weld residual stress prediction: A review of the NeT TG4 simulation round robins part 2, mechanical analyses. Int. J. Press. Vessels Pip. 164, 130–165.
Sun, F., Meade, E.D., O'Dowd, N.P., 2019b. Strain gradient crystal plasticity modelling of size effects in a hierarchical martensitic steel using the Voronoi tessellation method. Int. J. Plast. 119, 215–229.
Sun, B., Palanisamy, D., Ponge, D., Gault, B., Fazeli, F., Scott, C., Yue, S., Raabe, D., 2019a. Revealing fracture mechanisms of medium manganese steels with and without delta-ferrite. Acta Mater. 164, 683–696.
Vasileiou, A.N., Smith, M.C., Balakrishnan, J., Francis, J.A., Hamelin, C.J., 2017. The impact of transformation plasticity on the electron beam welding of thick-section ferritic steel components. Nucl. Eng. Des. 323, 309–316.
Wu, M., Xin, R., Wang, Y., Zhou, Y., Wang, K., Liu, Q., 2016. Microstructure, texture and mechanical properties of commercial high-purity thick titanium plates jointed by electron beam welding. Mater. Sci. Eng. A 677, 50–57.
Wulfinghoff, S., Forest, S., Böhlke, T., 2015. Strain gradient plasticity modeling of the cyclic behavior of laminate microstructures. J. Mech. Phys. Solids 79, 1–20.
Yalçinkaya, T., Tandoğan, İ.T., Özdemir, İ., 2021. Void growth based inter-granular ductile fracture in strain gradient polycrystalline plasticity. Int. J. Plast. 147, 103123.
Zaefferer, S., Kuo, J.-C., Zhao, Z., Winning, M., Raabe, D., 2003. On the influence of the grain boundary misorientation on the plastic deformation of aluminum bicrystals. Acta Mater. 51 (16), 4719–4735.
Zecevic, M., Lebensohn, R.A., Capolungo, L., 2023. Non-local large-strain FFT-based formulation and its application to interface-dominated plasticity of nano-metallic laminates. J. Mech. Phys. Solids 173, 105187.
Zhao, Z., Ramesh, M., Raabe, D., Cuitino, A., Radovitzky, R., 2008. Investigation of three-dimensional aspects of grain-scale plastic surface deformation of an aluminum oligocrystal. Int. J. Plast. 24 (12), 2278–2297.